

Dissipationless Circulating Currents and Fringe Magnetic Fields Near a Single Spin Embedded in a Two-Dimensional Electron Gas

Adonai R. da Cruz^{1,*} and Michael E. Flatté^{2,1,†}

¹*Department of Applied Physics, Eindhoven University of Technology, Eindhoven 5612 AZ, The Netherlands*

²*Department of Physics and Astronomy, University of Iowa, Iowa City, Iowa 52242, USA*

(Dated: November 15, 2021)

Theoretical calculations predict the dissipationless circulating current induced by a spin defect in a two-dimensional electron gas with spin-orbit coupling. The shape and spatial extent of these dissipationless circulating currents depends dramatically on the relative strengths of spin-orbit fields with differing spatial symmetry, offering the potential to use an electric gate to manipulate nanoscale magnetic fields and couple magnetic defects. The spatial structure of the magnetic field produced by this current is calculated and provides a direct way to measure the spin-orbit fields of the host, as well as the defect spin orientation, *e.g.* through scanning nanoscale magnetometry.

Single spins associated with point defects in solid-state materials are promising candidates for qubits and novel quantum spintronic devices for communication, sensing, and information processing [1–5]. Isolated magnetic dopants embedded in two-dimensional electron gases (2DEG) with spin-orbit coupling (SOC) can be electrically and optically addressed [6–8] and coherently manipulated. Control of the relative phases of defect spin wave functions through manipulation of the spin-spin coupling enables spin-based quantum computation[1–3]. To date most spin-spin couplings are achieved either through dipolar magnetic fields arising from the spin [9, 10], which are difficult to tune, or through photonic coupling [11], which is effective for much longer distances. The magnetic moment of a bare spin is modified by the spin-orbit interaction of the host, leading to proposals for single-spin control via g tensor manipulation [12–19], however the effects on nanoscale dipolar fields and the consequences for coupling spins remain unexplored.

Here we derive the dissipationless circulating current surrounding a spin embedded in a 2DEG with spin-orbit coupling, and show that these effects are significant and their spatial structure is detectable by current nanoscale magnetometry[20–23]. The spin-orbit interaction in a 2DEG can be modified with a perpendicular electric field (without dissipative current flow) thus we further propose that modifying these magnetic fields provides a method of electrically tuning spin-spin interactions to produce quantum entangling gates. Our results rely on a derivation of the 2DEG’s current operator that identifies the critical role of effective spin-orbit vector potentials in correctly producing currents that are dissipationless. We compare diverse hosts for these phenomena including semiconductor quantum wells (QWs) and surfaces (*e.g.*, the electron accumulation layer in InAs [24–26]), oxide interfaces (*e.g.*, LaAlO₃/SrTiO₃[27]), atomically thin ma-

terials (*e.g.*, BiSb[28] and WSeTe[29]) and films (*e.g.*, LaOBiS₂[30]). Our expressions for circulating currents connect to other fundamental features of an electron gas interacting with localized magnetic moments, including Friedel oscillations of charge and spin densities [31, 32], the Dzyaloshinskii-Moriya interaction [33] and long-range Ruderman Kittel-Kasuya-Yosida [34–37] interactions between defects. Measurement of the spatial structure of this current can be achieved by probing the magnetic fringe field above the surface with nanoscale scanning magnetometry (*e.g.* using nitrogen-vacancy (NV) centers in diamond [20–23]), which have achieved spatial resolution in the nanometer range and field sensitivity (tens to hundreds of nT), on the order of the features calculated here. Another option relies on recent advances in electron ptychography for direct sensing[38].

Central to our results is the derivation of the current operator associated with the effective Hamiltonian describing a 2DEG with SOC,

$$H = \frac{\hbar^2 k^2}{2m^*} + \alpha (\sigma_x k_y - \sigma_y k_x) + \beta (\sigma_x k_x - \sigma_y k_y). \quad (1)$$

The spin orbit fields linear in crystal momentum \mathbf{k} emerge from both the crystal’s bulk inversion asymmetry (BIA, with coefficient β)[39] and the inversion asymmetry of the heterostructure (SIA, with coefficient α , which can be tuned by applied electric fields perpendicular to the 2DEG plane)[40]. We derive the current operator (see Supplementary Material [41]) from the steady-state continuity equation $\partial_t n + \nabla \cdot \mathbf{j} = 0$ and group the spin-orbit terms together in an effective spin-dependent vector potential \mathbf{A}_{so} . The expected value of the charge current is evaluated using the Green’s function (GF) scattering formalism,

$$\mathbf{j}(\mathbf{r}) = -\frac{e\hbar}{2\pi m^*} \text{Im} \int_{E_{so}}^{E_f} (t_\uparrow - t_\downarrow) \left\{ i [(\nabla G_{\uparrow\downarrow}^0) G_{\uparrow\downarrow}^0 - (\nabla G_{\downarrow\uparrow}^0) G_{\uparrow\downarrow}^0] - \frac{2e}{\hbar} (\mathbf{A}_{so}^{\uparrow\downarrow} G_{\uparrow\downarrow}^0 - \mathbf{A}_{so}^{\downarrow\uparrow} G_{\uparrow\downarrow}^0) G_{\uparrow\uparrow}^0 \right\} dE. \quad (2)$$

where $G^0(\mathbf{r}, \mathbf{r}')$ are the 2DEG retarded GFs, t_σ are the defect T-matrix elements with spin projection σ , E_{so} is the energy minimum of the 2DEG, E_f is the Fermi energy (determined by the electron density n) and the effective vector potential

$$\mathbf{A}_{so} = \frac{\hbar k_{so}}{e} \left\{ [\sigma_x \cos(\theta - \tau) - \sigma_y \sin(\theta + \tau)] \hat{r} + [\sigma_x \sin(\theta - \tau) - \sigma_y \cos(\theta + \tau)] \hat{\theta} \right\}, \quad (3)$$

with $\tau = \tan(\alpha/\beta)$ and $k_{so} = (m^*/\hbar^2)\sqrt{\alpha^2 + \beta^2}$.

$$G^0(\mathbf{r}; E) = -\frac{m^*}{2\pi^2\hbar^2} \int_{\theta-\pi/2}^{\theta+\pi/2} d\theta_k \left\{ \frac{\sigma_0}{Q} [k_+ I_1(k_+\rho) + k_- I_1(k_-\rho)] - i \frac{[U_x \sigma_x - U_y \sigma_y]}{Q \sqrt{f_\tau}} [k_+ I_2(k_+\rho) - k_- I_2(k_-\rho)] \right\}, \quad (6)$$

where $\rho = r \cos(\theta_k - \theta)$, $U_x = \cos(\theta_k - \tau)$, $U_y = \sin(\theta_k + \tau)$ and $I_{1/2}(k_\pm \rho)$ are closed-form functions [42]. Changes in the convexity of the outer contour, $k_\pm(\theta_k, \tau)$, for a given energy $E = \sqrt{\hbar^2 k_E^2}/2m^*$ are driven by the SOC ratio τ through $f_\tau(\theta_k)$ and produce important consequences for electronic properties in real space, such as enhanced electron beam formation for transport along symmetry axes[42].

We now embed a defect with spin employing the Dyson equation for the new GF perturbed by a magnetic potential. For simplicity we assume that the electron is scattered isotropically with an incident wavelength large enough to not sense the spatial structure of the potential (s -wave approximation), although our treatment is easily generalized to more complex situations. The T-matrix[43]

$$t_\sigma = \left(\frac{4i\hbar^2}{m^*} \right) \left[e^{(2i\delta_\sigma)} - 1 \right], \quad (7)$$

where the scattering phase-shift of the spin channel σ , δ_σ , is related to the defect local density of states through the Friedel sum rule [31] and encodes its charge and spin state. Here we assume an energy independent T-matrix for a spin-polarized defect with magnetization fixed along the out-of-plane axis (z axis), where the the spin-down state is fully occupied and does not participate in scattering processes ($\delta_\downarrow = 0$) and the partially occupied spin-up channel has a resonant level at the Fermi energy ($\delta_\uparrow = \pi/2$).

We now show results for a 2DEG formed by the electron accumulation layer at a InAs(001) surface [24] using $k_{so} = 0.2 \text{ nm}^{-1}$, $E_f = 10 \text{ meV}$ and $m^* = 0.023 m_0$. The low effective mass, strong spin-orbit coupling, and high

The retarded Green's function from Eq. (1) is [42]

$$g^0(\mathbf{k}; E) = \left(\frac{2m^*}{\hbar^2} \right) \frac{(k_E^2 - k^2)\sigma_0 - 2k_{so}k[U_x\sigma_x - U_y\sigma_y]}{k_E^4 - 2k^2[k_E^2 + 2k_{so}^2 f_\tau(\theta_k)] + k^4} \quad (4)$$

where $k_E^2 = 2m^*E/\hbar^2$ and $f_\tau(\theta_k) = 1 + \sin(2\tau)\sin(2\theta_k)$. The poles of the Green's function correspond to Fermi contours of the two spin-split subbands at energy E and is obtained from the roots of the denominator,

$$k_\pm = Q \pm k_{so} \sqrt{f_\tau(\theta_k)}, \quad Q = \sqrt{k_E^2 + k_{so}^2 f_\tau(\theta_k)}. \quad (5)$$

The representation of the GF in real space is obtained by Fourier transform of Eq. (4),

Landé g factor makes this a promising system in which to detect these orbital features since the current magnitude is proportional to $(\alpha^2 + \beta^2)^{1/2}/m^*$ [Eq. (2)]. Conversion factors for different materials are provided in Table I for the spatial dimensions (d_{fac}) and for the magnetic field strengths (B_{fac}) in the figures below.

Figure 1 shows the current density induced by a magnetic defect at the origin ($\mathbf{r}_0 = 0$) with spin projection along the [001] out-of-plane direction, calculated from Eq. (2). For $\alpha \gg \beta$, corresponding to $\tau = \pi/2$ [Fig. 1(a)], the isotropic dispersion relation implied by a θ_k -independent f_τ allows for an analytical solution to Eq. (6) in terms of Hankel functions of the first kind [32, 44]. The current then has only an angular component and oscillates with two characteristic lengths, reminiscent of Friedel oscillations, given by $\lambda_f = \pi/k_f$ and $\lambda_{so} = \pi/k_{so}$.

The emergence of the anisotropy in the dispersion relation when both α and β are relevant [Fig. 1(bc)] drastically changes the spatial structure of the circulating current compared to Fig. 1(a), stretching the features along the symmetry axes. For $\alpha/\beta > 0$ a stronger current density focuses along the $\theta = 3\pi/4$ direction [Fig. 1(b)] and rotates by 90° focusing along $\theta = \pi/4$ when $\alpha/\beta < 0$ [Fig. 1(c)], a consequence of an interfering contribution of stationary points[42]. The currents are equal but rotate in opposite directions for values of $\tau = \pi/4 \pm \delta$ ($\tau = \pi/4$ corresponds to $\alpha = \beta$), as shown in Fig. 1(bc). This change in rotation would invert the orbital magnetization around the spin (see Supplementary Material[41]). We note that when $\alpha = \beta$, the extra SU(2) symmetry implies a fixed spin quantization axis independent of \mathbf{k} , making the 2DEG GF of Eq. (6) spin-diagonal upon a global spin rotation [45] and thus both contributions to

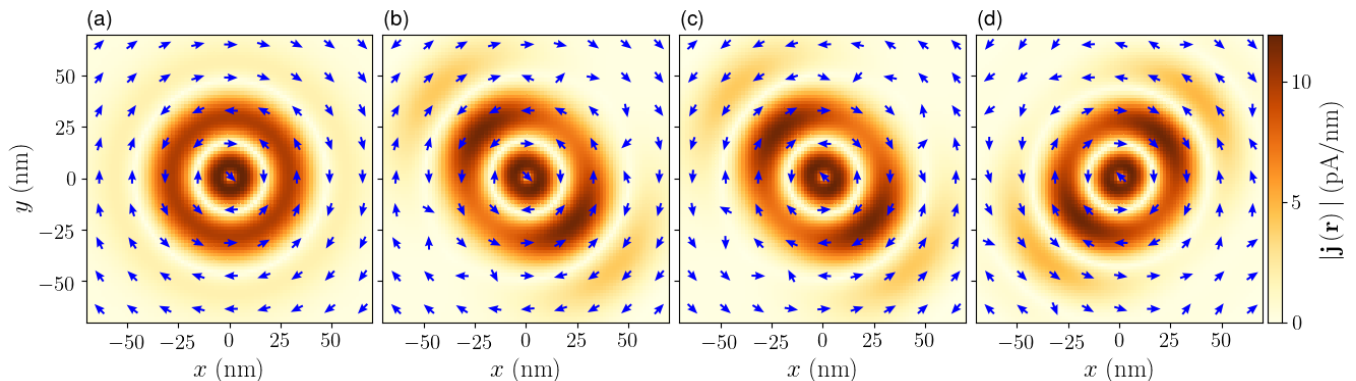


FIG. 1. Current density induced by a magnetic point defect with spin pointing perpendicular to an InAs 2DEG. (a) SIA dominated regime ($\beta = 0$, $\tau = \pi/2$) showing angular symmetry. (b-d) $\beta \neq 0$; the angularly anisotropic circulating current stretches along the symmetry axis $\theta = 3\pi/4$ for $\alpha/\beta > 0$ (bc) or along $\theta = \pi/4$ for $\alpha/\beta < 0$ (d). Opposite circulation direction of $\tau = \pi/4 + 0.1$ (b) from $\tau = \pi/4 - 0.1$ (c); current vanishes for $\tau = \pi/4$ ($\alpha = \beta$).

the current in Eq. (2) vanish.

The spatial structure of the orbital magnetization density associated with these circulating currents can be calculated in analogy with classical electrodynamics using[46] $\mathbf{m}_{orb}(\mathbf{r}) = (1/2)\mathbf{r} \times \mathbf{j}(\mathbf{r})$; the current density is obtained from Eq. (2). To compare both the orbital and spin contributions to the defect-induced magnetization we calculate the latter by

$$\mathbf{m}_{spin}(\mathbf{r}) = -\frac{\mu_B}{\pi} \text{Im} \int_{E_{so}}^{E_f} \boldsymbol{\sigma} G(\mathbf{r}; E) dE, \quad (8)$$

where μ_B is the Bohr magneton and $\boldsymbol{\sigma}$ are the Pauli matrices. We note that orbital momentum quenching is reduced for systems with strong spin-orbit coupling, allowing a comparable orbital magnetization to the spin magnetization. As shown in Fig. 2, although the spin-orbit fields alter both orbital and spin magnetization densities around a magnetic defect, the orbital magnetization has distinct spatial oscillations and is highly sensitive to the SOC ratio τ .

The magnetic fringe field above the 2DEG is obtained from the orbital magnetization density of a quantum-well with width d confined along the z -axis under hard-wall boundary conditions. By using the ground-state electron envelope function, $\phi(z) = (1/\sqrt{d}) \cos(\pi z/d)$, the previously calculated two-dimensional current density acquires a z -dependence of $\cos^2(\pi z/d)$, and a volumetric orbital magnetization density can be defined inside the quantum well.

In the region outside the magnetized volume, the magnetic fringe field is evaluated by $\mathbf{B} = -\mu_0 \nabla \Phi_{orb}(\mathbf{r})$, where $\mu_0 = 4\pi \times 10^{-7} \text{ N/A}^2$ is the vacuum permeability and the scalar magnetic potential is[46]

$$\Phi_{orb}(\mathbf{r}) = \frac{1}{4\pi} \int d\mathbf{r}' \frac{\nabla' \cdot \mathbf{m}_{orb}(\mathbf{r}')}{|\mathbf{r} - \mathbf{r}'|}. \quad (9)$$

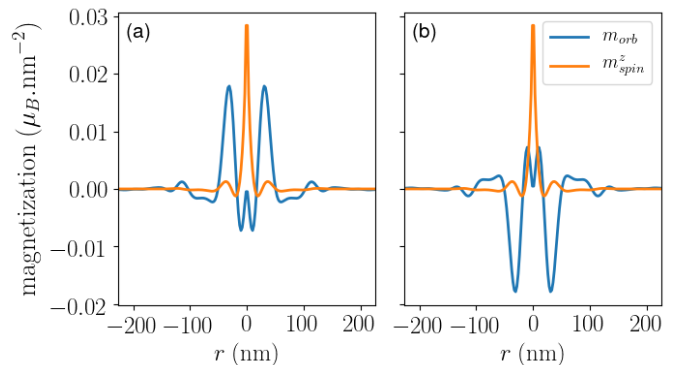


FIG. 2. Orbital (m_{orb}) and spin (m_{spin}^z) contributions to the 2DEG magnetization density showing the effects of the current circulation inversion between $\tau = \pi/4 - 0.1$ (a) and $\tau = \pi/4 + 0.1$ (b) along the $[1\bar{1}0]$ direction from a magnetic defect pointing perpendicular to the 2DEG.

Figure 3 shows the spatial distribution for each orbital fringe field component is calculated at 20 nm above a 10 nm InAs QW for this magnetic defect, and the largest values are tenths of μT , within the range of single NV diamond scanning magnetometry. In the left column of Fig. 3 the fringe field structure in the SIA dominated regime ($\tau = \pi/2$) reflects the radial symmetry of the circulating current in this regime, and the fields are generated by concentric current loops with current flowing in opposite directions. The BIA term induces angular anisotropy in the field distribution [Fig. 3(bdf)] providing a direct signature of the SOC ratio.

The magnitude of the orbital fringe field depends on the distance measured from the QW, *e.g.* decreasing fourfold at a distance of 20 nm from the InAs QW with respect to the field magnitude at the surface (Fig. 4), thus the close proximity achievable by nanoscale scanning probes can obtain even stronger responses within

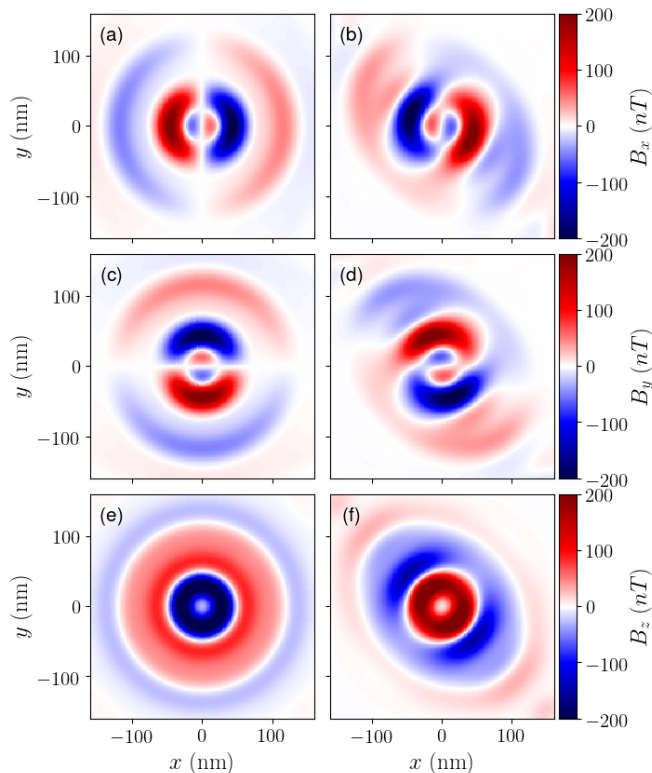


FIG. 3. Orbital fringe field components (ab) B_x , (cd) B_y and (ef) B_z 20 nm above the surface of an InAs quantum well with width 10 nm for a magnetic defect pointing perpendicular to the 2DEG. (ace) the SIA dominated regime, $\tau = \pi/2$. (bdf) for $\tau = \pi/8$.

its sensitivity range. The higher magnitude shown for currents with both SIA and BIA terms (crosses and blue lines in Fig. 4) occurs from higher currents due to the SOC-induced focusing effects. Furthermore, choices of different materials may lead to more detectable effects. Table I lists a variety of materials with either stronger magnetic fields or larger-scale spatial features, along with some more challenging materials that would have both (*i.e.* BiSb). In Table I we keep the two-dimensional electron density fixed to be $4 \times 10^{11} \text{ cm}^{-2}$, and note that the features can also become larger (or smaller) for different electron densities.

The circulating dissipationless current associated with a single spin in a 2DEG formed in non-centrosymmetric materials with SOC creates spatial features highly sensitive to the underlying tunable spin-orbit field and the defect-spin direction, a reminiscent of the anisotropic dispersion relation and Friedel oscillations. Nanoscale scanning probe magnetometry, or potentially electron ptychography, is sufficiently sensitive to measure the spatially-resolved orbital contribution to the magnetic moment of a single spin. The spatial structure of the defect magnetic moment affects its coupling to nearby rapidly oscillating fields from e.g. nuclear-spins, with im-

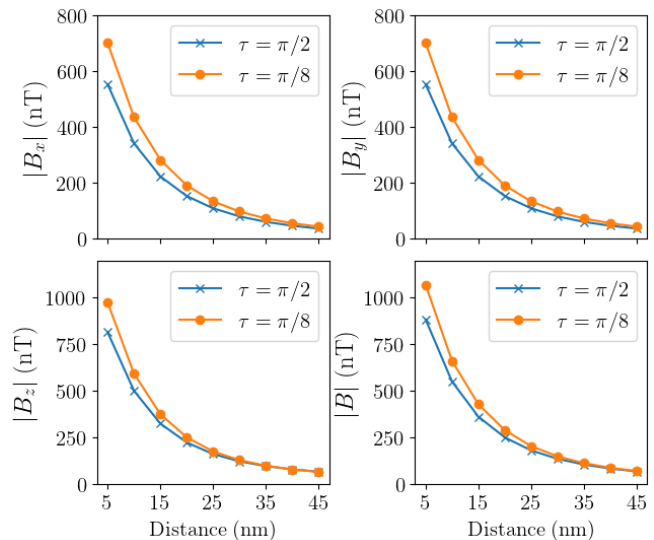


FIG. 4. Maximum magnitude of the orbital fringe field components B_x , B_y and B_z and total magnetic field B calculated at different distances above a 10 nm InAs QW. Shown for $\beta = 0$, $\tau = \pi/2$ (crosses and blue lines) $\beta \neq 0$, $\tau = \pi/8$ (circles and orange lines).

TABLE I. Parameters and conversion factors for the spatial dimension (d_{fac}) and magnetic field strength (B_{fac}) for different materials. We assume the QW width is 10 nm.

Material	$m^*(m_0)$	α (meV.nm)	d_{fac}	B_{fac}
InAs[47]	0.023	50	1.0	1.0
GaAs/AlGaAs[48]	0.067	4.8	3.58	0.096
LAO/STO[27]	2.2	3.4	0.15	0.068
InGaAs/InAlAs[49]	0.05	40.0	0.57	0.8
BiSb[28]	0.002	230	2.5	4.6
LaOBiS ₂ [30]	0.07	478	0.034	9.56
WSeTe [29, 50]	0.81	92	0.015	1.84

plications for spin-dynamics and coherent control of single spin states [51].

We acknowledge support from the ITN 4PHOTON Marie Skłodowska Curie Grant Agreement No. 721394.

* adonaire@gmail.com

† michael.flatte@mailaps.org

- [1] B. E. Kane, Nature (London) **393**, 133 (1998).
- [2] D. Loss and D. P. DiVincenzo, Phys. Rev. A **57**, 120 (1998).
- [3] D. D. Awschalom, N. Samarth, and D. Loss, eds., *Semiconductor Spintronics and Quantum Computation* (Springer Verlag, Heidelberg, 2002).
- [4] K. Ichimura, Opt. Commun. **196**, 119 (2001).
- [5] G. Wolfowicz, F. J. Heremans, C. P. Anderson, S. Kanai, H. Seo, A. Gali, G. Galli, and D. D. Awschalom, Nat. Rev. Mater. **6**, 906 (2021).
- [6] T. Matsui, C. Meyer, L. Sacharow, J. Wiebe, and

- R. Wiesendanger, Phys. Rev. B **75**, 165405 (2007).
- [7] D. H. Lee and J. A. Gupta, Science **330**, 1807 (2010).
- [8] R. C. Myers, M. H. Mikkelsen, J.-M. Tang, A. C. Gossard, M. E. Flatté, and D. D. Awschalom, Nat. Mater. **7**, 203 (2008).
- [9] T. Gaebel, M. Domhan, I. Popa, C. Wittmann, P. Neumann, F. Jelezko, J. R. Rabeau, N. Stavrias, A. D. Greentree, S. Praver, J. Meijer, J. Twamley, P. R. Hemmer, and J. Wrachtrup, Nature Phys **2**, 408 (2016).
- [10] G. D. Fuchs, G. Burkard, P. V. Klimov, and D. D. Awschalom, Nature Phys **7**, 789 (2011).
- [11] E. Togan, Y. Chu, A. S. Trifonov, L. Jiang, J. Maze, L. Childress, M. V. G. Dutt, A. S. Sørensen, P. R. Hemmer, A. S. Zibrov, and M. D. Lukin, Nature **466**, 730 (2010).
- [12] Y. Kato, R. C. Myers, D. C. Driscoll, A. C. Gossard, J. Levy, and D. D. Awschalom, Science **299**, 1201 (2003).
- [13] J. Pingenot, C. E. Pryor, and M. E. Flatté, Applied Physics Letters **92**, 222502 (2008).
- [14] J. Pingenot, C. E. Pryor, and M. E. Flatté, Phys. Rev. B **84**, 195403 (2011).
- [15] M. D. Schroer, K. D. Petersson, M. Jung, and J. R. Petta, Phys. Rev. Lett. **107**, 176811 (2011).
- [16] S. Takahashi, R. S. Deacon, A. Oiwa, K. Shibata, K. Hirakawa, and S. Tarucha, Phys. Rev. B **87**, 161302(R) (2013).
- [17] N. Ares, G. Katsaros, V. N. Golovach, J. J. Zhang, A. Prager, L. I. Glazman, O. G. Schmidt, and S. De Franceschi, Applied Physics Letters **103**, 263113 (2013).
- [18] A. Crippa, R. Maurand, L. Bourdet, D. Kotekar-Patil, A. Amissé, X. Jehl, M. Sanquer, R. Laviéville, H. Bohuslavskiy, L. Hutin, S. Barraud, M. Vinet, Y.-M. Niquet, and S. De Franceschi, Phys. Rev. Lett. **120**, 137702 (2018).
- [19] A. Ferrón, S. A. Rodríguez, S. S. Gómez, J. L. Lado, and J. Fernández-Rossier, Phys. Rev. Research **1**, 033185 (2019).
- [20] M. W. Doherty, N. B. Manson, P. Delaney, F. Jelezko, J. Wrachtrup, and L. C. Hollenberg, Physics Reports **528**, 1 (2013).
- [21] M. S. Grinolds, S. Hong, P. Maletinsky, L. Luan, M. D. Lukin, R. L. Walsworth, and A. Yacoby, Nat. Phys. Lett. **9**, 215 (2013).
- [22] F. Casola, T. Van Der Sar, and A. Yacoby, Nat. Rev. Mater. **3**, 17088 (2018).
- [23] C. L. Degen, F. Reinhard, and P. Cappellaro, Rev. Mod. Phys. **89**, 035002 (2017).
- [24] M. Noguchi, K. Hirakawa, and T. Ikoma, Phys. Rev. Lett. **66**, 2243 (1991).
- [25] G. R. Bell, T. S. Jones, and C. F. Mcconville, Appl. Phys. Lett **71**, 3688 (1997).
- [26] L. Canali, J. W. G. Wildöer, O. Kerkhof, and L. P. Kouwenhoven, Appl. Phys. A **66**, 113 (1998).
- [27] A. Fête, S. Gariglio, C. Berthod, D. Li, D. Stornaiuolo, M. Gabay, and J. M. Triscone, New J. Phys. **16**, 112002 (2014).
- [28] S. Singh and A. H. Romero, Phys. Rev. B. **95**, 165444 (2017).
- [29] Q.-F. Yao, J. Cai, W.-Y. Tong, S.-J. Gong, J.-Q. Wang, X. Wan, C.-G. Duan, and J. H. Chu, Phys. Rev. B **95**, 165401 (2017).
- [30] Q. Liu, Y. Guo, and A. J. Freeman, Nano Lett. **13**, 5264 (2013).
- [31] J. Friedel, Nuovo Cimento **2**, 287 (1958).
- [32] S. Lounis, A. Bringer, and S. Blügel, Phys. Rev. Lett. **108**, 207202 (2012).
- [33] F. Freimuth, S. Blügel, and Y. Mokrousov, Phys. Rev. B **96**, 054403 (2017).
- [34] M. A. Ruderman and C. Kittel, Phys. Rev. **96**, 99 (1954).
- [35] T. Kasuy, Prog. Theor. Phys. **16**, 45 (1956).
- [36] K. Yosida, Phys. Rev. **106**, 893 (1957).
- [37] S. Chesi and D. Loss, Phys. Rev. B **82**, 165303 (2010).
- [38] Z. Chen, Y. Jiang, Y.-T. Shao, M. E. Holtz, M. Odstrčil, M. Guizar-Sicairos, I. Hanke, S. Ganschow, D. G. Schlom, and D. A. Muller, Science **372**, 826 (2021).
- [39] G. Dresselhaus, Phys. Rev. **199**, 556 (1955).
- [40] Y. A. Bychkov and E. I. Rashba, J. Phys. C: Solid State Phys. **17**, 6039 (1984).
- [41] See Supplemental Material for detailed calculations, which includes Refs. [], at <http://link.aps.org/supplemental/...>
- [42] D. H. Berman and M. E. Flatté, Phys. Rev. Lett **105**, 157202 (2010).
- [43] G. A. Fiete and E. J. Heller, Rev. Mod. Phys. **75**, 933 (2003).
- [44] J. Bouaziz, M. dos Santos Dias, F. S. M. Guimarães, S. Blügel, and S. Lounis, Phys. Rev. B **98**, 125420 (2018).
- [45] B. A. Bernevig, J. Orenstein, and S.-C. Zhang, Phys. Rev. Lett. **97**, 236601 (2006).
- [46] J. D. Jackson, *Classical electrodynamics*, 3rd ed. (Wiley, 1999).
- [47] D. Grundler, Phys. Rev. Lett **84**, 6074 (2000).
- [48] J. Yu, X. Zeng, S. Cheng, Y. Chen, Y. Liu, Y. Lai, Q. Zheng, and J. Ren, Nanoscale Res. Lett. **11**, 477 (2016).
- [49] J. Nitta, T. Akazaki, H. Takayanagi, and T. Enoki, Phys. Rev. Lett. **78**, 1335 (1997).
- [50] A. Bahrami, A. Houshang, L. Ju, M. Bie, J. Shang, P. Jamdagni, R. Pandey, and K. Tankeshwar, Nanotechnology **33**, 025703 (2021).
- [51] J. van Bree, A. Yu Silov, P. M. Koenraad, and M. E. Flatté, Phys. Rev. Lett **112**, 187201 (2014).